

Supporting Information:

Rotation and Negative Torque in Electrodynamically Bound Nanoparticle Dimers

Nishant Sule,^{†,§} Yuval Yifat,^{†,§} Stephen K. Gray,[‡] and Norbert F. Scherer^{*,†,¶}

[†]*James Franck Institute, The University of Chicago, 929 E. 57th Street, Chicago, Illinois
60637, USA*

[‡]*Center for Nanoscale Materials, Argonne National Laboratory, 9700 South Cass Avenue,
Argonne, Illinois 60439, USA*

[¶]*Department of Chemistry, The University of Chicago, 929 East 57th Street, Chicago,
Illinois 60637, USA*

[§]*These authors contributed equally to this work*

E-mail: nfschere@uchicago.edu

Experimental setup

The 150 nm Ag particles described in the text were trapped in a Gaussian laser beam that was focused through a microscope objective. A diagram of the trapping setup is shown in Figure S1. The setup consisted of a continuous wave Ti:Sapphire laser emitting linearly polarized (LP) light laser tuned to a wavelength of 790 nm. The beam was collimated and directed through a quarter wave plate, which is used to control its polarization, into a Nikon Ti inverted optical microscope and through a 60x IR corrected water immersion objective (Nikon 60x Plan APO IR water immersion objective, NA = 1.27). The incident

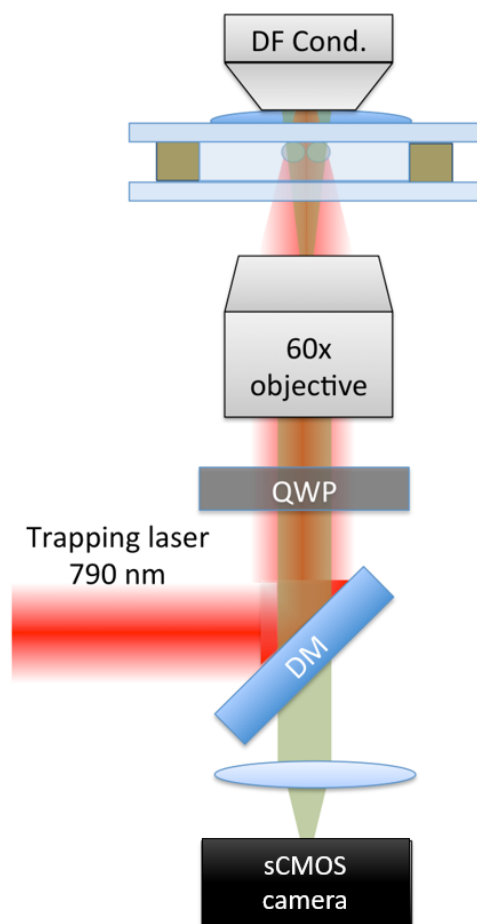


Figure S1: Diagram of experimental trapping setup described in the text. DF Cond. Dark field condenser, DM-Dichroic mirror. QWP Quarter wave plate. Dark-field (high N.A.) illumination that scatters from the Ag nanoparticles is collected by the microscope objective, spectrally filtered and imaged to a sCMOS array detector. The trapping laser reflected from a spatial light modulator (SLM; BNS/Meadowlark HSPDM512-785 nm that could be used for beam shaping.

power reported in the text (e.g. Fig. 2(b) in the main text) was measured before the dichroic mirror. The laser beam was focused into a sample cell that was filled with a solution of 150nm diameter silver nanoparticles coated with polyvinylpyrrolidone (PVP); the as purchased stock solution was diluted in 18M Ω de-ionized water in a ratio of 1:200. The beam was focused slightly below the top cover slip and had a measured FWHM of 450 nm (see Fig. 2(a) in the main text). In order to measure the FWHM of the trapping beam, we removed the IR filter before the camera and imaged the reflection of the beam off the cover slip. The particles were illuminated using a dark field condenser and the light they scattered in a dark-field configuration was captured by the objective and imaged onto a sCMOS camera (Andor Neo; 6.5 micrometer pixel size) with a total magnification of 90x, giving an effective pixel size of 72 nm. The particle motion was captured in a 50x50 pixel region of interest on the detector with an exposure time of 0.1ms at a frame rate of 2004 frames per second.

Characteristics of 150 nm diameter Ag nanoparticles

The particles used for the trapping experiments described in the main text are 150nm diameter polyvinylpyrrolidone (PVP) coated silver nanoparticles purchased from NanoComposix (NanoXact Silver KJW1882 0.02 mg/ml). The stock solution was diluted in DI water at a ratio of 1:200. Figure S2 presents the results of experiments we performed on the solution to determine the physical characteristics of the particles.

Fig S2(a) shows representative TEM images of the particles. The particles were drop cast on a copper grid and imaged using a FEI Tecnai F30 300kV FEG (s)TEM Electron Microscope using a magnification of x75K. We measured the absorbance of the stock solution using a Cary 5000 UV/Vis/IR spectrophotometer (Fig S2 b) and observed absorbance peaks at 440 nm and at 600 nm. These absorption peaks are interpreted as the dipole and quadrupole modes calculated from Mie scattering of a silver particle of the same diameter

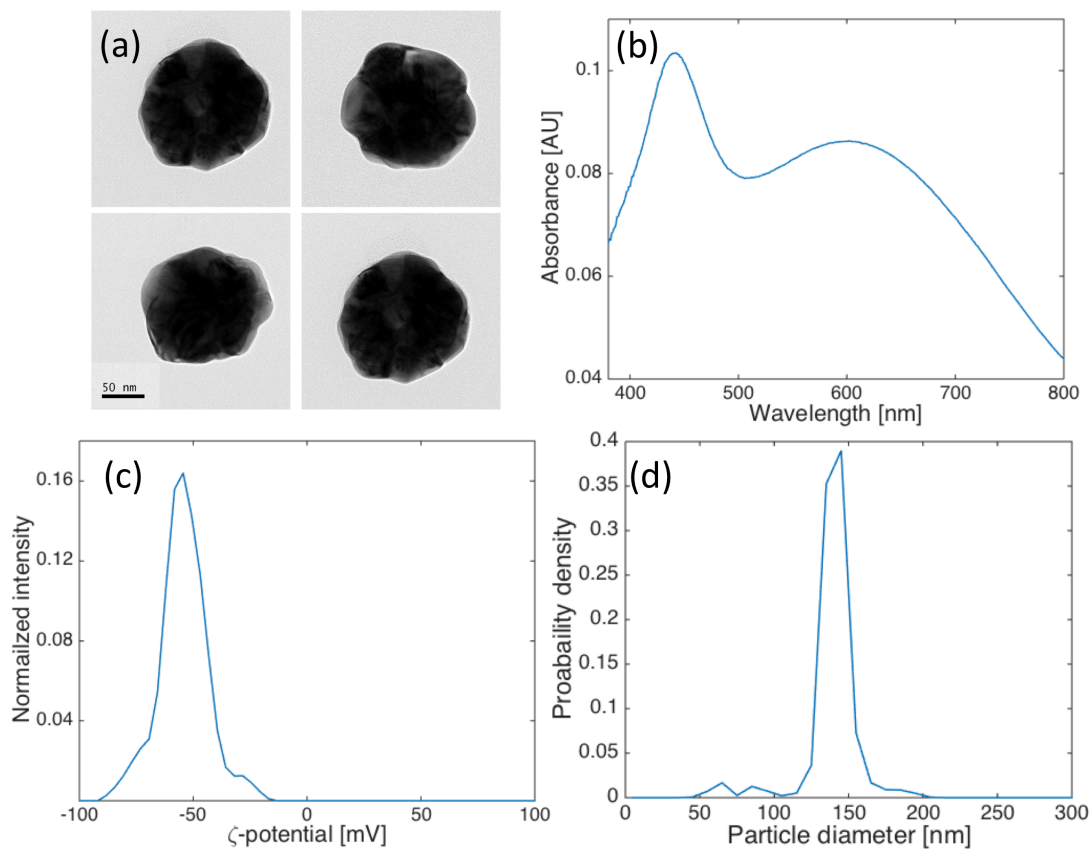


Figure S2: Results of analysis of 150 nm diameter Ag nanoparticles. (a) TEM images of nanoparticles dispersed on copper grid. Scale bar is 50 nm. (b) Extinction cross-section spectrum of original stock solution taken with a UV-Vis-IR spectrophotometer. Peak maxima at 440 nm and 600 nm correspond to the dipole and quadrupole Mie scattering modes of a 150 nm diameter silver particle immersed in water. (c) Probability distribution of a zeta potential measurement of the stock solution diluted in 18 M Ω nanopure water at a 1:200 ratio. The mean value is -54.3mV. (d) Probability distribution of particle diameters of stock solution diluted in 18 M Ω nanopure water at a ratio of 1:200. Data was obtained using a Malvern NanoSight nanoparticle tracking analysis system. Mean diameter value is 148 nm.

immersed in water¹.

The zeta-potential of the trapped particles shown in Fig S2(c) was measured using a Malvern NanoZS zetasizer. The measurement was performed on a sample diluted from the stock solution in 18 M Ω nanopure water at a ratio of 1:200. The mean zeta-potential from the measurement is -54.3 mV.

The distribution of particle diameters was measured using a Malvern NanoSight NS300 particle sizer which records videos of the particles and uses particle tracking methods to estimate the particle diameter from their diffusive behavior. The resulting probability distribution of particle sizes is shown in Fig S2(d). We determined that the mean particle hydrodynamic radius of the particles was 148 ± 5 nm for a sample diluted from the stock solution at a ratio of 1:200 by fitting the distribution of the particle diameters with a Gaussian function.

Simulation method

The motion of Ag nanoparticles in circularly polarized (CP) focused Gaussian beams are simulated using an in-house method that combines FDTD with a Langevin equation integrator (the ED-LD method).² We have previously used this method to simulate the trapping, interparticle interactions, and dynamics in linearly polarized focused Gaussian traps² as well as linearly polarized optical ring vortex traps³ The method works as follows. The optical forces on the nanoparticles are calculated using the Maxwell stress tensor by propagating 12–15 time periods (*i.e.* optical cycles) of the incident focused Gaussian beam in the simulation domain. The optical forces are used in the Langevin equation as a driving force and the particle positions are calculated from integrating the Langevin equation. After the particle has moved by more than one particle radius (typically 5 Langevin time steps), the optical forces are recalculated and the aforementioned steps are repeated.

The CP focused Gaussian beam is introduced in the FDTD simulation using the scattered

field method,^{4,5} where the incident electric field is defined as:⁶

$$E(r, \phi, z) = E_0 \frac{ikf e^{ikf}}{4\sqrt{2}} \sqrt{\frac{1}{n_m}} \begin{bmatrix} I_{00} + I_{02} \cos 2\phi \mp I_{02} \sin 2\phi \\ I_{02} \sin 2\phi \mp i(I_{00} - I_{02} \cos 2\phi) \\ -2iI_{01} \cos \phi \mp 2I_{01} \sin \phi, \end{bmatrix} \quad (\text{S1})$$

in Cartesian coordinates, where $k = 2\pi/\lambda$ is the wavenumber of the trapping beam, f is the focal length of the lens, $E_0 = \sqrt{2I_0/c\epsilon_0 n_m}$ is the electric field amplitude in terms of the beam intensity, I_0 , and n_m , the refractive index of the medium. The column vector denotes the Cartesian components of the CP incident electric field where the negative (positive) sign represents left (right) handed circular polarization. The integrals I_{00} , I_{01} , and I_{02} are defined as

$$I_{00} = \int_0^{\theta_{max}} f_w(\theta) \sqrt{\cos \theta} \sin \theta (1 + \cos \theta) J_0(k\rho \sin \theta) e^{ikz \cos \theta} d\theta, \quad (\text{S2a})$$

$$I_{01} = \int_0^{\theta_{max}} f_w(\theta) \sqrt{\cos \theta} \sin^2 \theta J_1(k\rho \sin \theta) e^{ikz \cos \theta} d\theta, \quad (\text{S2b})$$

$$I_{02} = \int_0^{\theta_{max}} f_w(\theta) \sqrt{\cos \theta} \sin \theta (1 - \cos \theta) J_2(k\rho \sin \theta) e^{ikz \cos \theta} d\theta. \quad (\text{S2c})$$

Here, $f_w(\theta) = e^{-\frac{1}{f_0^2} \frac{\sin^2 \theta}{\sin \theta_{max}}}$ is a pupil filter function, $f_0 = w_0/f \sin \theta_{max}$ is the filling factor of the lens, $\sin \theta_{max} = NA/n_m$, and w_0 is the beam waist. The J_n 's are the n th order Bessel functions of the first kind. We used the same NA as the experimental setup (i.e. $NA = 1.27$) and assume the beam diameter incident on the focusing lens to be 1.1 mm.

We use a time step between 0.1 μs and 0.5 μs for integrating the Langevin equation, and assume a temperature of 320 K, which takes into account local heating of the nanoparticles. The value of the dynamic viscosity of water at 320 K (0.8 Pa s) was used.

Image analysis

All the experimental videos were tracked and linked using the open source Mosaic particle tracking plugin for imageJ,⁷ which uses non-linear fitting of a Gaussian function to the intensity distribution of the pixels. However, due to the small particle sizes and the small separation between them, and due to the high rotation frequency in some of the videos, the raw tracking data exhibited two systematic errors that required correction.

First, the small size of the particles on the detector, which was usually 2-4 pixels FWHM, and their separation (2-5 pixels for the experiments in which the particles are in the near field) meant that the tracking had to be done using the algorithm's smallest possible window size for particle identification and Gaussian fitting/centroid localization. Thus, we identified the particles using a Gaussian window with a diameter of $W=2R+1$ pixels and a radius of $R=1$ pixel (essentially a Swiss cross) to maximize the identification of individual particles. If the tracking was done with a larger window, such as one with a window radius of 2 or especially 3 pixels, the fitted Gaussian was larger than each individual particle and tended to misidentify both particles as a single particle. We occasionally observed such misidentification even when we used a small Gaussian window. Such events were not taken into account in the analysis. See for example Fig 1c in the main text, where the points in which the RCP measurement (blue connected dots) shows fewer points than the LCP (red connected dots). Frames in which both particles were not identified were ignored in the analysis, and thus do not appear in the figure.

However, such a small window size is susceptible to a Nyquist undersampling error that results in a systematic error known as pixel locking^{8,9} in which the particle positions are biased towards the center of the pixel. This can be seen in Figure S3a, which displays the set of decimal parts of the tracked particle locations from one experimental video gathered into a single "meta-pixel". This distribution shows that the particle positions are severely biased towards the center of the pixel (blue points are individual localizations), introducing a localization error that (strongly) effects the calculation of interparticle separation and angle

values. The pixel locking error is clearly seen in distribution of the interparticle separations (blue curve in Figure S3c) calculated from the tracked data. Due to the pixel locking error, the distance is discontinuous, as evident in the spikes in the distribution. The distribution should be smooth.

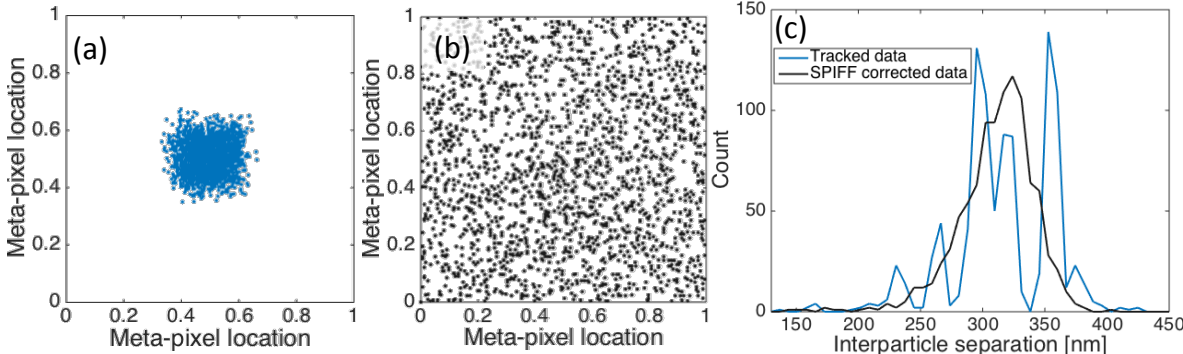


Figure S3: Pixel locking, error and SPIFF correction. (a,b) Decimal part of the pixel localization in a "meta-pixel". The localizations are from the tracked data of an experimental video of two particles in the near-field before (a; blue) and after (b; black) SPIFF correction. (c) Histogram of interparticle separation values before and after SPIFF correction obtained from the same experimental data. Data shown in this figure were obtained from tracking an experimental video of an electrodynamically bound dimer (EBD) rotating with input optical power of 7mW. Data was taken from an experimental video with 1000 frames and 2000 particle localizations.

The pixel locking bias was removed by using the Single Pixel Interior Filling Function (SPIFF) method, which is a corrective algorithm introduced by Burov et al.¹⁰ Application of the SPIFF algorithm caused the meta-pixel distribution to become uniform (see Figure S2b). Moreover, the errors in interparticle separation were corrected (see black curve in Figure S2c). A comprehensive analysis of the effects of pixel-locking and its correction is given in Yifat et al.¹¹

The second issue was the frame-to-frame linking of the tracked particle positions in a video. The linking method we used (part of the Mosaic suite in ImageJ) assumed that the particle motion was Brownian. Thus, a specific particle and its location in frame n will be linked to the particle in frame $n + 1$ that is closest to its original position, calculated as the Cartesian distance of the tracked positions between the frames. In the case of two

rotating particles in the near-field that we can mark as P_a and P_b , this means that when the rotational velocity is sufficiently high (above $90^\circ/\text{frame}$ on average) a given particle, P_a will be farther away in the next frame from its original position than particle P_b and the linking algorithm will switch their identifications. Indeed, we often saw such a “skipping” of the particle identification between frames; that is P_a in frame n was linked to P_b in frame $n + 1$ and vice versa, leading to errors in the linking of particles across frames and, of course, in the calculated rotational velocity.

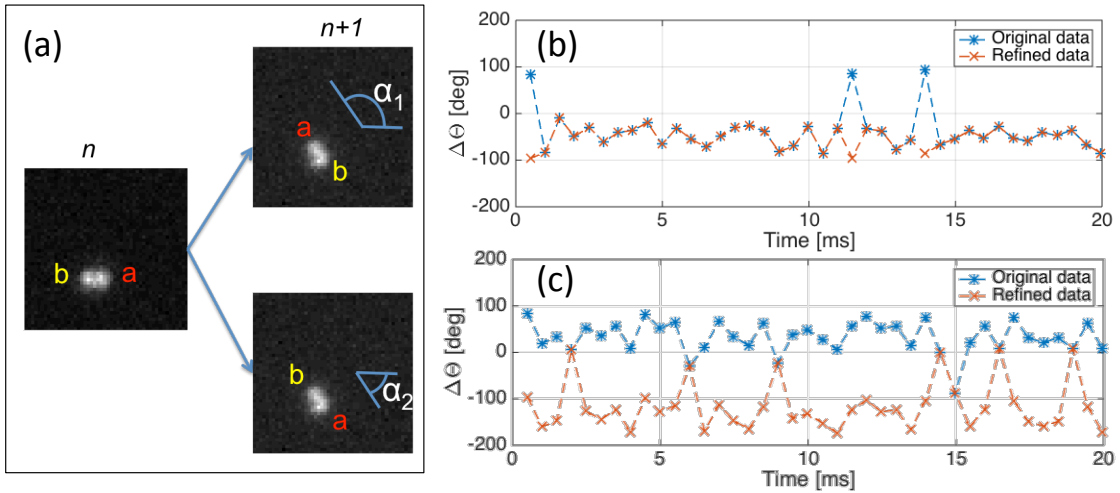


Figure S4: (a) Illustration of refined linking to accommodate directed vs. purely Brownian motion. There are two possible interparticle angles for frame $n + 1$ (marked as α_1 and α_2 in the figure) once the particles in frame n are identified and localized. The identification of the particles is done in accordance to the expected rotation direction. In this example we select the particle identities corresponding to either α_1 if the rotation is counter-clockwise or α_2 if it is clockwise. (b) Representative results of the refined linking for experimental data with small mean rotational velocity (incident optical power is 9 mW). Note that the refined linking does not affect the majority of the data points. (c) Representative results of biased tracking for experimental data with a large rotational velocity (incident optical power is 14 mW). In this case most of the tracked frames are affected and correctly assigned by the refined linking.

To overcome this misidentification effect, we implemented a refined linking method that, starting from the first frame, linked the particles in subsequent frames by calculating both possible interparticle angles and identified the particles by choosing the angle that better matches the observed dynamics. An example of this method is illustrated in Figure S4a. The

identities of the two particles in frame n are known, and there are two linking possibilities leading to two possible interparticle angles in frame $n + 1$. The choice of angle is made by taking into account the direction of motion (CW or CCW) and setting a threshold angle that determines the largest angle that will be refined by the method (i.e. no refinement is done for angles larger than this value). The effect of the refinement is shown in Figure S4b,c for videos of particles with small and large rotational velocity that occurs at correspondingly low and high optical powers.

Total optical torque

The time averaged optical torque on an object in a circularly polarized electric field is given by^{12,13}

$$\langle \vec{\tau} \rangle = \vec{r} \times \langle \vec{F} \rangle + \frac{1}{2} \langle \vec{p} \times \vec{E}^* \rangle + \frac{1}{2} \langle \vec{B} \times \vec{H}^* \rangle, \quad (\text{S3})$$

where \vec{r} represents the position of the object relative to the axis around which the torque is calculated, \vec{F} is any external force on the object, \vec{p} is the polarization density vector, \vec{E} is the total electric field, and \vec{B} , \vec{H} are the magnetic flux density and magnetic field, respectively. The first term in Eq. S3 represents the extrinsic part of the optical torque as it depends on the location of the torque axis and the external force on the EBD. In the case of our EBD and an incident plane wave, the torque axis is coincident with the z -axis (See Figure 3a). Therefore, $\vec{r} = 0$ and the first term on the right hand side is also zero. The second term depends on the angle between of the polarization density vector and the total electric field and therefore represents an intrinsic part of the optical torque corresponding to the spin angular momentum transferred from CP light. Because of the isotropic magnetic permeability of Ag nanoparticles the last term on the right hand side is zero. Finally, the dipole approximation requires a self-field correction for the electric field term.^{12,13} Thus, the

torque for spherical EBD's under the dipole approximation is given by

$$\langle \vec{\tau} \rangle = \frac{1}{2} \Re \left[\vec{p} \times (\overline{\alpha}_0^{-1} \vec{p})^* \right], \quad (\text{S4})$$

where $\overline{\alpha}_0$ is the effective polarizability matrix composed of the parallel and perpendicular polarizabilities with α from Eq. 1 replaced by α_0 .

Interaction matrix elements

The polarization density vector (\vec{p}) in Eq. S3 can be written as $\vec{p} = \overline{\alpha} \vec{E}$, where $\overline{\alpha}$ represents the effective polarizability of the object (*e.g.* the nanoparticle EBD).

$$\overline{\alpha} = \begin{bmatrix} \alpha_{\parallel} & 0 & 0 \\ 0 & \alpha_{\perp} & 0 \\ 0 & 0 & \alpha_{\perp} \end{bmatrix} \quad (\text{S5})$$

For the EBD, we take into account the plasmonic resonance of the Ag nanoparticles through their complex permittivity, ϵ_p , which is embedded in the single-particle polarizability, α . As seen from Eq. 1a,b, the effective polarizability of the dimer along and perpendicular to the dimer axis (α_{\parallel} and α_{\perp} , respectively) is a function of separation, δ due to the separation-dependent interaction matrix elements A and B (Eq. 2a,b). These interaction matrix elements change sign as a function of separation as shown in Figure S5. As a result of retardation effects, the separation-dependent sign of the effective polarizability gives rise to the negative torque for certain separations.

Converting fields to the coordinate frame of the EBD

The effective polarizability $\overline{\alpha}$ is defined in the EBD frame, *i.e.*, with components parallel

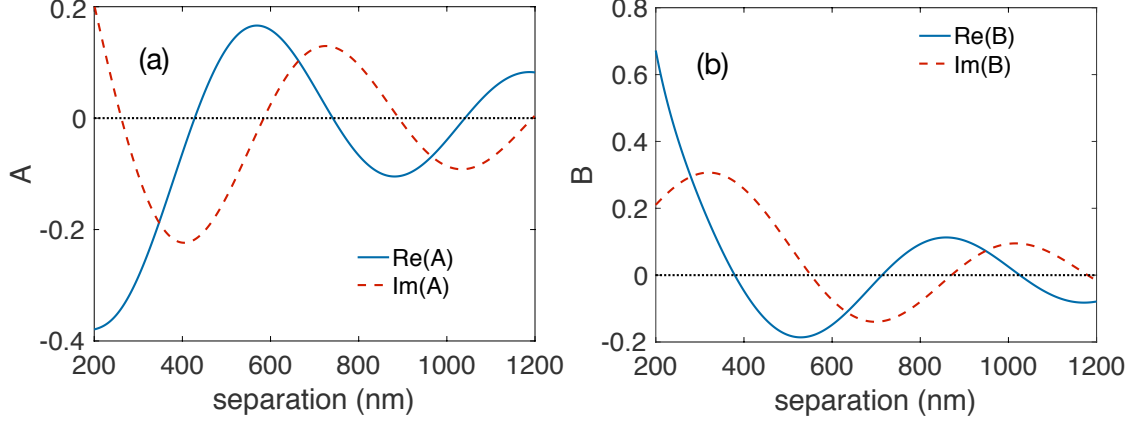


Figure S5: Real and imaginary parts of the interaction matrix elements (a) A and (b) B as a function of interparticle separation. See Eq. 2a,b in the main text for the expressions for A and B .

(α_{\parallel}) and perpendicular (α_{\perp}) to its axis. However, the electric field, \vec{E} , is defined in the lab frame. Say, the field at an instant of time makes an angle Ω with respect to the lab frame. Then, we convert the electric field to the EBD frame by multiplying with the rotation matrix.

$$\begin{bmatrix} E'_x \\ E'_y \\ E'_z \end{bmatrix} = \begin{bmatrix} \cos \phi & \sin \phi & 0 \\ -\sin \phi & \cos \phi & 0 \\ 0 & 0 & 1 \end{bmatrix} \begin{bmatrix} 1 \\ i \\ 0 \end{bmatrix} E_0 e^{ikz}, \quad (\text{S6})$$

where $\phi = \Omega - \theta$. The polarization density \vec{p}' in the EBD frame is then,

$$\begin{bmatrix} p'_x \\ p'_y \\ p'_z \end{bmatrix} = \begin{bmatrix} \alpha_{\parallel} & 0 & 0 \\ 0 & \alpha_{\perp} & 0 \\ 0 & 0 & \alpha_{\perp} \end{bmatrix} \begin{bmatrix} \cos \phi \pm i \sin \phi \\ -\sin \phi \pm i \cos \phi \\ 0 \end{bmatrix} E_0 e^{ikz} \quad (\text{S7})$$

Torque expression

The time averaged optical torque on the EBD is given by Eq. S4. Using Eq. S7, and

some algebra we obtain the following.

$$\langle \vec{\tau} \rangle = \frac{|E_0|^2}{2} \Re \left\{ \begin{bmatrix} \alpha_{\parallel}(\cos \phi \pm i \sin \phi) \\ \alpha_{\perp}(-\sin \phi \pm i \cos \phi) \\ 0 \end{bmatrix} \times \begin{bmatrix} \frac{\alpha_{\perp}^*}{\alpha_{0,\perp}^*}(\cos \phi \mp i \sin \phi) \\ \frac{\alpha_{\parallel}^*}{\alpha_{0,\parallel}^*}(-\sin \phi \mp i \cos \phi) \\ 0 \end{bmatrix} \right\} \quad (\text{S8})$$

Taking the cross product on the right-hand side, we obtain the expression below.

$$\langle \vec{\tau} \rangle = \frac{|E_0|^2}{2} \Re \left[\alpha_{\parallel} \frac{\alpha_{\perp}^*}{\alpha_{0,\perp}^*} (\cos \phi \pm i \sin \phi) (-\sin \phi \mp i \cos \phi) - \alpha_{\perp} \frac{\alpha_{\parallel}^*}{\alpha_{0,\parallel}^*} (-\sin \phi \pm i \cos \phi) (\cos \phi \mp i \sin \phi) \right]. \quad (\text{S9})$$

Using trigonometric identities this expression can be simplified to give the angle independent expression for the torque given in Eq. 3 of the main text. If we assume a linearly polarized incident field then the torque expression becomes a function of orientation, proportional to $\sin 2\phi$, which can only orient the EBD along the direction of polarization and cannot continuously rotate it.

Relation between angular velocity and torque in an over-damped system

The rotational Langevin equation for a particle can be written as,

$$I \frac{d^2\theta(t)}{dt^2} = \tau(t) - \gamma \frac{d\theta(t)}{dt} + \eta(t), \quad (\text{S10})$$

where I is the moment of inertia, θ is the angular position, τ is the torque, γ is the rotational friction, and η is the equivalent stochastic rotational thermal torque (a Gaussian white noise). For an over-damped system, the inertia term is set to zero. Defining $\omega = d\theta/dt$ and

rearranging we get the relation between the angular velocity, ω , and the torque, τ

$$\omega(t) = \frac{\tau(t) + \eta(t)}{\gamma}. \quad (\text{S11})$$

Taking the average on both sides, we find that $\langle\omega(t)\rangle = \gamma^{-1}\langle\tau(t)\rangle$ since $\langle\eta(t)\rangle = 0$. The angular velocity and torque thus have a linear relation in the overdamped limit. This linear relationship between ω and τ allows us to make the comparison shown in Fig. 4b.

Example of a negative torque event

A frame-by-frame example of a negative torque event for two 150 nm diameter silver particles in a loosely focused Gaussian trap (*i.e.* a Gaussian trap that was created by placing an iris before the objective and has a waist that is wider than that of a tightly focused Gaussian beam) is given in Figure S6. This particular event is highlighted in the main text in Figure 4(c,d). These frames are also shown in Movie S6.

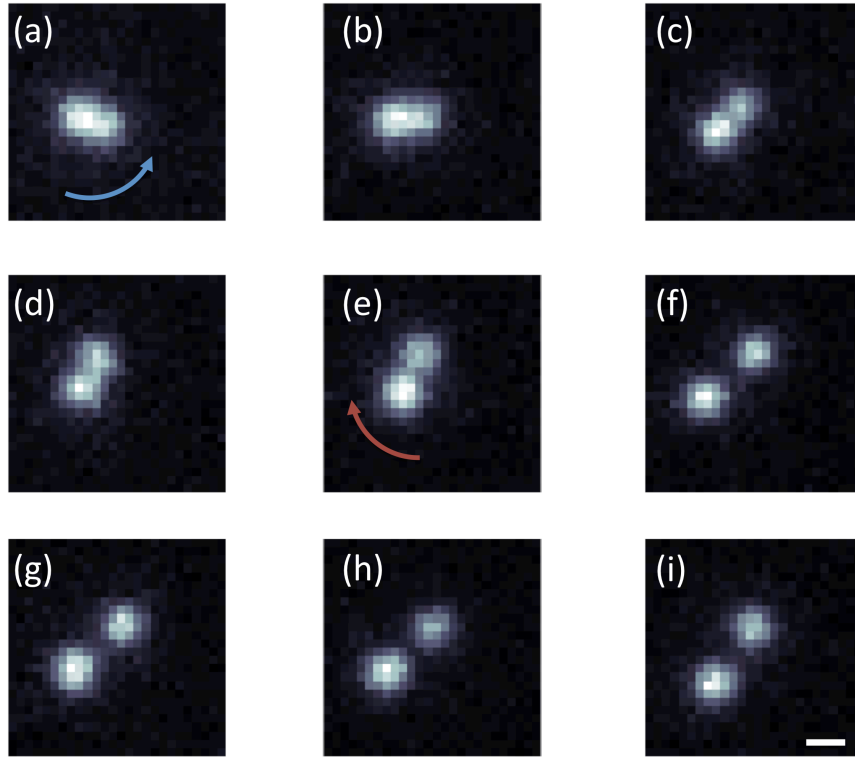


Figure S6: Experimental frame-by-frame example of negative torque of an EBD composed of two 150 nm Ag nanoparticles. The particles are trapped in a circularly polarized loosely focused Gaussian trap. Panels (a-d) show the CCW rotation of the pair when the particles are in the near-field. In panel (e) the particles are separated by 400 nm and as a result the rotation direction is reversed. This is evident in the change of rotation direction from panel (e) to (f). In panels (f-i) the particles are at optical binding distance and their rotation is small. The instantaneous rotation value of the EBD and its absolute angle are given in Fig 4(c-d) in the main text. The frame rate is 2004 FPS. Scale bar is 360 nm.

Statistical analysis of negative torque

As was explained in the main text, the difficulty in measuring negative torque in our experiments is that its maximal value occurs when the interparticle separation is roughly 400 nm, which is the transition state position position between the energetically more favorable near-field and the optical binding regions. Analyzing more than 4×10^4 frames from several experimental videos taken under similar experimental conditions yields 125 frames in which the particles are separated by about 400 nm (see Figure S7 and the natural logarithm of the probability distribution presented in Figure 4f of the main text). In those frames we calculate an average experimental negative torque of $\theta_{expt} = -85$ rad/sec (corresponding to -2.4 degrees/frame). This value is marked by the arrow in Figure 4d in the main text.

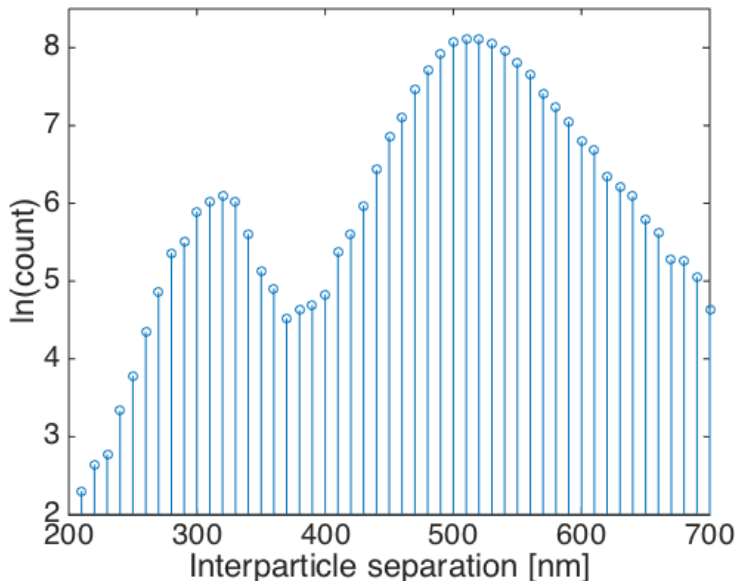


Figure S7: Natural log of the counts of measured events as a function of interparticle separation for the experimental data presented in Fig. 4 of the main text.

Each particle of the EBD is subject to Brownian motion in addition to optically induced forces such as the gradient forces and those stemming from interparticle scattering. At larger separation, the interparticle scattering is weak and Brownian motion is dominant. To establish the statistical validity of the negative rotations being due to negative torque we estimated the statistical likelihood of experimental negative rotation caused only by

Brownian particle motion. Therefore we simulated the Brownian motion experienced by the particle pair as it is manifested as changes in the interparticle angle, $\Delta\theta$, in order to model the fluctuations we observe experimentally. We started by placing particle 1 at (0,0) and particle 2 at varying distances between 150 and 700 nm with a step of 10 nm, and an initial interparticle angle of 0^0 . For each of the starting positions we simulated a set of 10^4 random Brownian displacements, for both particles 1 and 2, and calculated the post-displacement interparticle angles and separations. The calculation of the Brownian motion was based on the particle radius (75 nm), the viscosity of the medium (taken as 0.8 Pa.s), the temperature ($T = 320K$) and a time step of $0.5ms$, equivalent to the camera frame rate. The resulting changes in interparticle angle $\Delta\theta$ as a function of separation are shown in Fig S8a.

Figure S8a shows the effect of interparticle separation on the change in interparticle angle. A slight change in the perpendicular position of the particles results in a larger difference in the interparticle angle for smaller interparticle separations. This can be understood intuitively: if one of the particles is moved 50 nm perpendicular to the interparticle axis due to Brownian motion, the effect on the interparticle angle will be more pronounced when the particles are in the near-field, than when they are further away. This is evident as the decrease in the magnitude of the standard deviation of the angles for a given separation (dashed curves) as the separation increases, while the mean difference in interparticle angle (black circles) remains equal to zero.

Figure S8b shows how the simulated standard deviations compare to the experimental ones. The simulated standard deviation values were fitted to the experimental ones at large interparticle separations by multiplying them by a constant of 0.62. This scaling can arise from several factors: the local temperature and viscosity are different near the particles than in the simulation data; the particle motions in the experiment see more correlation than the independent particle motion that is assumed in the simulation; the experiment allows restricted 3D motion vs. 2D motion in the simulation. However, the important point is that the trend of the simulated standard deviation agrees with the experimental one

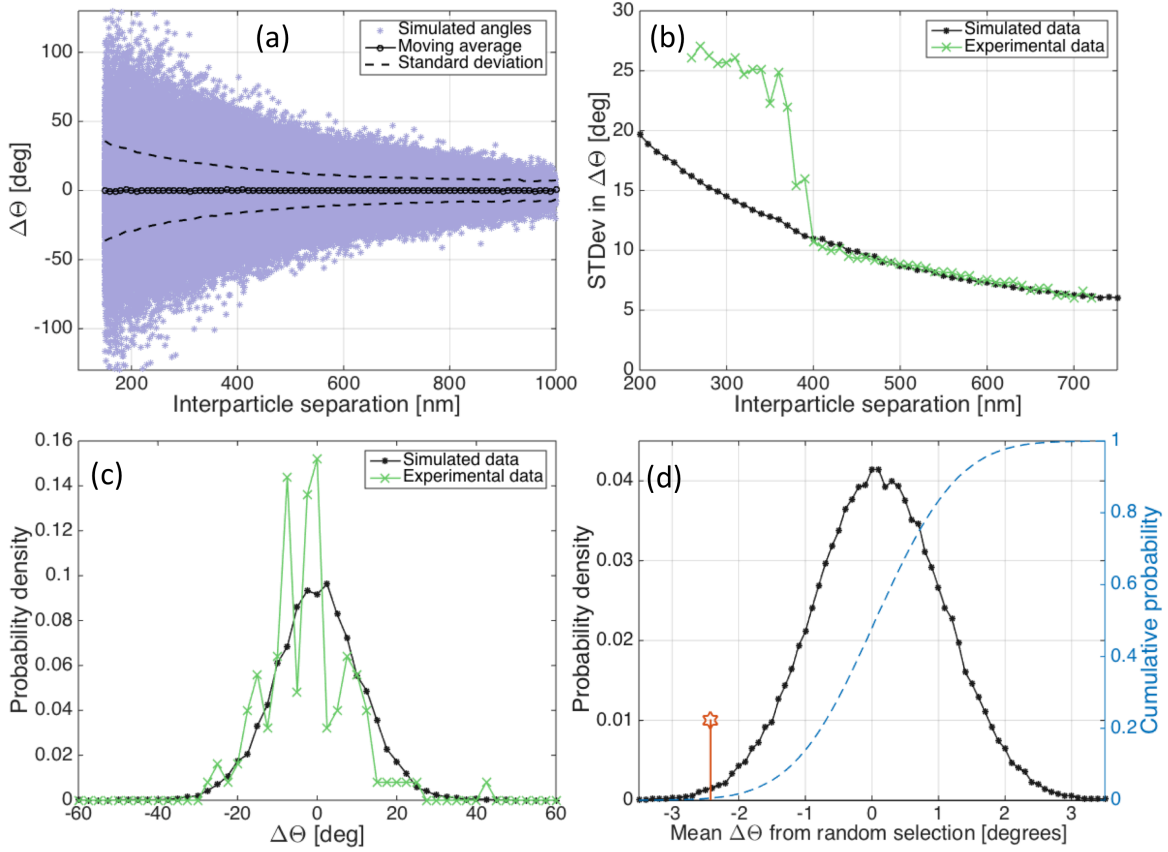


Figure S8: Statistical analysis of negative rotational velocity. (a) Change in interparticle angle, $\Delta\theta$, as a function of interparticle separation resulting from Monte-Carlo simulation of two particles subjected to Brownian motion. Note that the mean value of the change in interparticle angle (represented by black circles) is equal to zero, regardless of separation, but the standard deviation (represented by the black dashed lines) decreases with increasing separation. (b) Standard deviation values of $\Delta\theta$ fluctuations from the simulations overlaid with the standard deviation from experimental data (green connected dots). (c) Probability density of simulated $\Delta\theta$ chosen for the events with a separation of 400 ± 5 nm for the simulated (black) and experimental (green) data. (d) Probability density (black connected dots) and cumulative probability density (blue dashed line) of mean value calculated for 10^5 random selections of 125 data points from the simulated $\Delta\theta$ curve (shown in panel (c)). The red marker shows the position of the experimentally observed angular rate of change of $\Delta\theta_{expt} = -2.4$ degrees/frame.

extremely well when the particles are in the range of separations corresponding to optical binding distances where the scattering forces are small and their trajectories are dominated by Brownian motion.

Figure S8c shows the $\Delta\theta$ distributions at a separation of around 400 nm taken from the simulated data along with the corresponding experimental data. The simulated distribution is composed of about 10^4 data points, while the experimental distribution has 125 data points. While the distribution from Brownian fluctuations of $\Delta\theta$ in the simulation is Gaussian distributed about $\Delta\theta = 0$, the experimental data are biased to negative values.

We used the extracted probability distribution to assess the likelihood of obtaining a negative torque experimental value if the particle motion is dominated by Brownian noise. We simulated the possible outcomes of such an experiment by randomly selecting 125 points from the $\Delta\theta$ distribution shown in Figure S8c, and calculating the mean value of the change in interparticle angle: $\Delta\theta_{sim}$. We repeated the random selection of $\Delta\theta_{sim}$ 10^5 times and display its distribution in Figure S8d along with the cumulative probability and a marker for the experimentally measured value $\Delta\theta_{expt}$.

The cumulative probability density in Figure S8d shows that if the particles are subject only to Brownian motion, the probability of observing the experimental value of $\Delta\theta_{expt} = -2.4$ degrees/frame is 0.1%. In fact, from analysis of the cumulative distribution (shown as the blue dashed line in Figure S8d) we can say that if the motion of the particles is strictly Brownian, the likelihood of measuring an experimental result of $\Delta\theta_{expt} \leq -2.4$ deg/frame is 0.45%. *Thus, we assert that the observed negative velocity $\Delta\theta_{expt}$ and hence negative torque is not due to random Brownian fluctuations with a confidence level approaching 3σ . Instead, the measured negative torque is a physical manifestation of the electrodynamic interactions discussed in the text.*

Observation of Negative torque in 200 nm Ag diameter nanoparticle EBDs

The negative torque was further verified by repeating the trapping experiments on 200 nm diameter Ag particles coated in PVP (NanoComposix NanoXact Silver DAC1326 0.02 mg/mL). Other than the particle diameter, the conditions of the experiment were identical to those used for the 150 nm diameter particles. The particles were diluted in 18 M Ω nanopure water at a 1:200 ratio and were trapped in a circularly polarized, loosely focused Gaussian beam. The incident power was measured to be 25 mW after the iris that was used for beam shaping and defining the tightness of focus.

We recorded and tracked 8×10^4 experimental frames of the two particles captured in the trap and used the same methods described in the main text to analyze the resulting data. The mean instantaneous angular velocity (ω) measured as a function of interparticle separation, is shown in Figure S9a.

Qualitatively, the trapping experiments showed similar behavior to that seen for the 150 nm diameter particles. When the particles were in the near-field, they formed an electro-dynamically bound dimer and rotated as a bound pair, whereas at optical binding distances the average ω was zero. We observed a peak corresponding to negative torque located at 410 nm with a mean value of $\Delta\theta_{expt} = -69\text{rad/sec}$, or $\Delta\theta_{expt} = -2\text{ degrees/frame}$.

A significant difference was the scarcity of events in the near-field compared to the 150 nm particle experiments. This is evident in Fig S9b that shows the logarithm of the probability density function (which represents the potential of mean force). We observe that for the majority of captured frames, the particles are at optical binding separation. Thus, the likelihood of finding them at the near-field is significantly reduced compared to the experiments done with 150 nm diameter particles (compare to figure 4(f) in the main text). As a result, we found only 63 frames of the particles at the separation that leads to negative torque (410nm) out of more than 8×10^4 experimental frames.

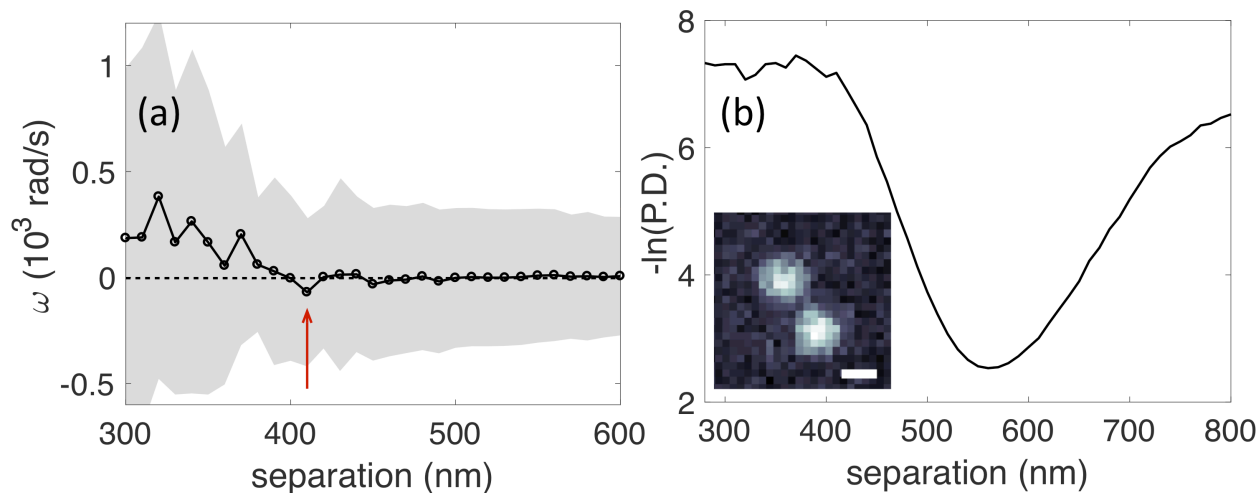


Figure S9: Experimental observation of negative torque in a 200 nm diameter Ag nanoparticle EBD. (a) Experimentally determined average angular velocity as a function of particle separation showing a signature of negative torque on the EBD at a separation of 410 nm. The grey shaded area represents the standard deviation from the mean value of ω . The red arrow indicates the transition point in the particle separation where the average ω is negative due to negative torque. (b) Negative natural log of the probability density $[-\ln(\text{P.D.})]$, representing the potential of mean force as a function of interparticle separation for the experimental data presented in panel (a). Inset is a representative frame of the two particles separated by 580 nm. Scale bar is 360 nm.

The differences in the observed position of the negative torque and in the shape of the PMF are due to the size of the particles. Since the particles are larger, their near-field interaction is less stable due to the Coulomb repulsion between them. In addition, their size leads to more complicated (Mie type) scattering. Their dipole mode is red-shifted, and their quadrupole mode is stronger compared to the 150 nm particles. As a result, the scattering interaction between them and the scattering retardation is significantly different than that of 150 nm particles. This leads to a change in the separations at which the negative torque is formed and in a smaller likelihood of near field interaction between the particles compared to the 150 nm case.

Next, we used the experimental data to assess the statistical significance of the negative torque for the 200 nm diameter particles. This was done using the same methods described in the Statistical analysis for negative torque section and Figure S8 above. The results of the analysis are shown in Figure S10. Similar to the analysis performed for 150 nm diameter Ag nanoparticles, we simulated the effect of Brownian motion on a non-interacting particle pair. We then calculated the interparticle angle of the particle pair at varying separations. Figure S10a shows the effect of interparticle separation on the change in interparticle angle for random Brownian displacements. The results are similar to those seen in Fig S8a, and the slight difference between them is due to the larger particle radius in this section, which leads to slightly smaller Brownian displacement values.

In Fig S10b we compare the standard deviation of the experimental rotation to that obtained from simulation. The simulated standard deviations were fitted to the experimental ones at large interparticle separations by multiplying them by a constant of 0.82.

Fig S10c shows the $\Delta\theta$ distributions at a separation of 410 ± 5 nm taken from the simulated data along with the corresponding experimental data. The simulated data is composed of about 10^4 points in the distribution, while the experimental data has 63 distribution points. While the distribution from Brownian fluctuations of $\Delta\theta$ in the simulation is Gaussian distributed about $\Delta\theta = 0$, the experimental data are biased to negative values.

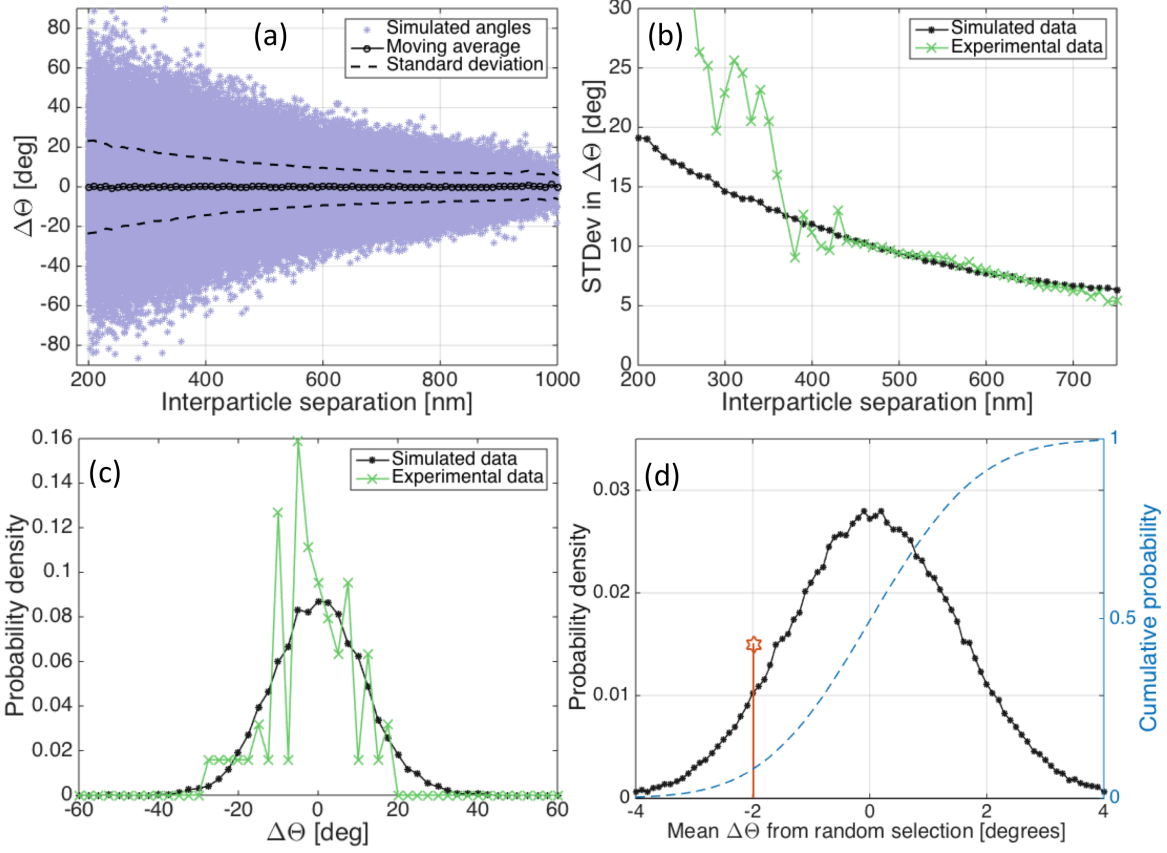


Figure S10: Statistical analysis of negative rotational velocity of 200 nm diameter Ag EBDs. (a) Change in interparticle angle, $\Delta\theta$, as a function of interparticle separation resulting from Monte-Carlo simulation of two particles subjected to Brownian motion. Note that the mean value of the change in interparticle angle (represented by black circles) is equal to zero, regardless of separation, but the standard deviation (represented by the black dashed lines) decreases with separation. (b) Standard deviation values of $\Delta\theta$ from the simulations overlaid with the standard deviation from experimental data (green connected dots). (c) Probability density of simulated $\Delta\theta$ chosen for the events with a separation of 410 ± 5 nm for the simulated (black) and experimental (green) data. (d) Probability density (black connected dots) and cumulative probability density (blue dashed line) for 10^5 random selections of 63 data points from the simulated $\Delta\theta$ curve (shown in panel (c)). The red marker shows the position of the experimentally observed angular rate of change of $\Delta\theta_{\text{expt}} = -2.0$ degrees/frame.

The likelihood of obtaining an experimental value for the negative torque for EBDs composed of 200 nm particles is shown in Fig S10d. The cumulative probability density in S10d shows that if the particles are subject only to Brownian motion, the probability of observing the experimental value $\Delta\theta_{expt} = -2.0$ deg/frame is 0.9%. From analysis of the cumulative distribution (shown as the blue dashed line in the Figure) we can say that if the motion of the particles is strictly Brownian, the likelihood of measuring an experimental result of $\Delta\theta_{expt} \leq -2.0$ deg/frame is roughly 8%. *Thus, following the same statistical methods we used in the Statistical analysis for negative torque section we find that the observed negative velocity $\Delta\theta_{expt}$, and hence negative torque, is not due to random Brownian fluctuations with a confidence level approaching 2σ .*

The difference in the confidence levels obtained for the 200 nm diameter EBDs compared to the analysis of the 150 nm diameter EBDs is due to the difference in their size, which makes it much less likely for the particles to fluctuate to near-field separations, and leads to a significant decrease in the number of observed events at separations smaller than the optical binding region. In addition, there is a difference in the scattering characteristics between the particles (i.e. the strength and frequency of their scattering cross section) that creates a different potential landscape between them.

Nonetheless, despite the differences in particle behavior, we are able to observe negative torque with a large statistical significance also for 200 nm diameter silver particles. This result further strengthens our confidence in the results obtained for the 150 nm diameter EBDs.

List of videos

Movie S1 – Experimental video of two 150 nm diameter Ag nanoparticles trapped in the near-field region in a linearly polarized focused Gaussian beam.

Movie S2 – Simulated trajectories of two 150 nm Ag nanoparticles illuminated by a circularly polarized focused Gaussian beam (both right-handed and left-handed circular

polarization).

Movie S3 – Experimental video of two 150 nm diameter Ag nanoparticles trapped in a left-handed circularly polarized loosely focused Gaussian beam.

Movie S4 – Experimental video of two 150 nm diameter Ag nanoparticles trapped in the near-field region and rotating clockwise in a right-handed circularly polarized focused Gaussian beam.

Movie S5 – Experimental video of two 150 nm diameter Ag nanoparticles trapped in the near-field region and rotating counter-clockwise in a left-handed circularly polarized focused Gaussian beam.

Movie S6 – Example of a negative torque event taken from an experimental video of two 150 nm diameter Ag nanoparticles trapped in a left-handed circularly polarized loosely focused Gaussian beam.

References

- (1) Horvath, H. *Journal of Quantitative Spectroscopy and Radiative Transfer* **2009**, *110*, 787–799.
- (2) Sule, N.; Rice, S. A.; Gray, S. K.; Scherer, N. F. *Opt. Express* **2015**, *23*, 29978–29992.
- (3) Figliozzi, P.; Sule, N.; Yan, Z.; Bao, Y.; Burov, S.; Gray, S. K.; Rice, S. A.; Vaikuntanathan, S.; Scherer, N. F. *Phys. Rev. E* **2017**, *95*, 022604.
- (4) Sun, W.; Pan, S.; Jiang, Y. *Journal of Modern Optics* **2006**, *53*, 2691–2700.
- (5) Kong, S. C.; Simpson, J. J.; Backman, V. *IEEE Microwave and Wireless Components Letters* **2008**, *18*, 4–6.
- (6) Novotny, L.; Hecht, B. *Principles of Nano-Optics*; Cambridge University Press, 2006.

- (7) Sbalzarini, I. F.; Koumoutsakos, P. *Journal of Structural Biology* **2005**, *151*, 182–195.
- (8) Crocker, J. C.; Hoffman, B. D. *Methods in cell biology* **2007**, *83*, 141–178.
- (9) Feng, Y.; Goree, J.; Liu, B. *Review of scientific instruments* **2007**, *78*, 053704.
- (10) Burov, S.; Figliozzi, P.; Lin, B.; Rice, S. A.; Scherer, N. F.; Dinner, A. R. *Proc. Natl. Acad. Sci. U.S.A.* **2016**, 201619104.
- (11) Yifat, Y.; Sule, N.; Lin, Y.; Scherer, N. F. *arXiv:1705.07789* **2017**,
- (12) Chaumet, P. C.; Billaudeau, C. *Journal of Applied Physics* **2007**, *101*, 023106.
- (13) Simpson, S. H.; Hanna, S. *J. Opt. Soc. Am. A* **2009**, *26*, 625–638.